

Journal of Materials Chemistry A

Materials for energy and sustainability

Accepted Manuscript

This article can be cited before page numbers have been issued, to do this please use: P. D. Kolubah, H. Mohamed, M. N. Hedhili, M. B. Hassine, R. Ahmad, V. Velisoju, A. Emwas, P. Dally, L. Cavallo and P. Castaño, *J. Mater. Chem. A*, 2026, DOI: 10.1039/D6TA03240K.



This is an Accepted Manuscript, which has been through the Royal Society of Chemistry peer review process and has been accepted for publication.

Accepted Manuscripts are published online shortly after acceptance, before technical editing, formatting and proof reading. Using this free service, authors can make their results available to the community, in citable form, before we publish the edited article. We will replace this Accepted Manuscript with the edited and formatted Advance Article as soon as it is available.

You can find more information about Accepted Manuscripts in the [Information for Authors](#).

Please note that technical editing may introduce minor changes to the text and/or graphics, which may alter content. The journal's standard [Terms & Conditions](#) and the [Ethical guidelines](#) still apply. In no event shall the Royal Society of Chemistry be held responsible for any errors or omissions in this Accepted Manuscript or any consequences arising from the use of any information it contains.

1 **NiCoO_x@NiCo core-shell nanoparticles supported on Ti₃C₂T_x as**
2 **cathode electrocatalyst for microbial fuel cells**

3 Pewee D Kolubah^a, Hend Omar Mohamed^{a*}, Mohamed Nejjib Hedhi^b, Mohamed Ben Hassine^b, Rafia Ahmad^c,
4 Vijay K Velisoju^a, Abdul-Hamid Emwas^b, Pia Dally^a, Luigi Cavallo^c, Pedro Castaño^{a,d*}

5 ^a*Multiscale Reaction Engineering, KAUST Catalysis Center (KCC), King Abdullah University of Science and*
6 *Technology (KAUST), Thuwal, 23955-6900, Saudi Arabia.*

7 ^b*Core Labs, King Abdullah University of Science and Technology (KAUST), Thuwal, 23955-6900 Saudi*
8 *Arabia*

9 ^c*KAUST Catalysis Center (KCC), King Abdullah University of Science and Technology (KAUST), Thuwal,*
10 *23955-6900 Saudi Arabia*

11 ^d*Chemical Engineering Program, Physical Science and Engineering (PSE) Division, King Abdullah*
12 *University of Science and Technology.*

13
14 * Corresponding author: hend.mohamed@kaust.edu.sa, pedro.castano@kaust.edu.sa



15 **Abstract**View Article Online
DOI: 10.1039/D6TA03240K

16 The intrinsically sluggish oxygen reduction reaction (ORR) at platinum-group-metal-free cathodes
17 remains a key bottleneck for the practical deployment of microbial fuel cells (MFCs). $\text{Ti}_3\text{C}_2\text{T}_x$ MXene
18 is a promising conductive scaffold, yet its ORR activity is hindered by strong O_2 adsorption at Ti sites,
19 leading to sluggish kinetics at neutral pH. Here, we address this limitation by developing a targeted
20 chemical-reduction strategy that assembles NiCo alloy nanocores encapsulated in a thin NiCo-oxide
21 shell (~4 nm) onto $\text{Ti}_3\text{C}_2\text{T}_x$, forming a $(\text{NiCoO}_x@\text{NiCo})/\text{Ti}_3\text{C}_2\text{T}_x$ heterostructure catalyst. The core-shell
22 domains modulate the local electronic environment, lower the O_2 binding energy, and introduce
23 abundant active sites, thereby leveraging the high conductivity of $\text{Ti}_3\text{C}_2\text{T}_x$. As an air-cathode MFC
24 treating glucose-supplemented wastewater, the catalyst delivers a current density of 4.5 A m^{-2} and a
25 peak power density of 1.6 W m^{-2} , outperforming pristine $\text{Ti}_3\text{C}_2\text{T}_x$. This work establishes a generalizable
26 heterostructure design strategy for activating MXene-based catalysts toward efficient neutral-pH ORR,
27 bridging fundamental catalyst design with practical microbial fuel cell applications.

28 **Keywords:** MXene, Metal alloy catalysts, Oxygen electrolysis, Bioelectricity, Wastewater treatment



29 1. Introduction

30 The oxygen reduction reaction (ORR) is a cornerstone process in electrochemical energy
31 conversion technologies, yet its intrinsically sluggish kinetics often limit overall efficiency and
32 durability.¹ Achieving high ORR performance requires catalysts that simultaneously provide abundant
33 accessible active sites, optimized electronic structures, and long-term stability under operating
34 conditions.² These characteristics are especially vital for electrochemical energy technologies, such as
35 electrolyzers^{3,4}, microbial fuel cells (MFCs), enzymatic, and hydrogen fuel cells⁵⁻⁷, and rechargeable
36 batteries,⁸ where efficient oxygen electrochemistry under mild or neutral conditions remains a
37 significant challenge.

38 Among these technologies, MFCs have attracted increasing attention as a promising platform
39 for simultaneous wastewater treatment and electricity generation.⁹ However, their large-scale
40 implementation is constrained by the performance and cost of cathode catalysts.¹⁰⁻¹² Platinum-based
41 materials remain the benchmark for ORR, but their high cost, scarcity, and susceptibility to deactivation
42 limit practical deployment. Notably, the cathode alone accounts for nearly half of the total system cost,
43 underscoring the urgent need for efficient and durable platinum-group-metal-free alternatives.^{13,14}
44 Despite extensive progress in acidic and alkaline systems, the development of high-performance ORR
45 catalysts under neutral conditions relevant to MFCs remains comparatively underexplored.

46 Two-dimensional (2D) materials have emerged as promising candidates for electrocatalysis due
47 to their high surface area and tunable electronic properties.¹⁵ However, conventional 2D systems present
48 intrinsic limitations. For example, graphene exhibits excellent conductivity but lacks intrinsic catalytic
49 activity, requiring defect engineering or heteroatom doping to introduce active sites.¹⁶ Transition metal
50 dichalcogenides (TMDs), such as MoS₂, display catalytic activity primarily at edge sites, while their
51 basal planes remain largely inert, and their semiconducting nature restricts charge transfer.¹⁷ Similarly,
52 layered double hydroxides (LDHs) and related materials often suffer from low electrical conductivity,
53 limiting their performance in electron-transfer-driven reactions.¹⁸

54



55 MXenes, particularly $Ti_3C_2T_x$, have emerged as a distinctive class of 2D materials that combine metallic
56 conductivity, hydrophilic surfaces, and tunable surface terminations. These properties enable efficient
57 charge transport and provide opportunities to modulate the adsorption energetics of reaction
58 intermediates. Unlike many 2D systems, $Ti_3C_2T_x$ exhibits intrinsically accessible basal planes, making
59 it a promising platform for electrocatalysis. However, its ORR activity remains limited due to
60 excessively strong adsorption of oxygen intermediates (*O and *OH) at Ti sites, which impedes reaction
61 turnover, particularly under neutral-pH conditions¹⁹. Therefore, strategies that can precisely tune the
62 electronic structure and intermediate binding energies are essential to unlock its catalytic potential.^{19,20}

63 Heterostructure engineering offers an effective route to address this limitation. Incorporating
64 transition-metal alloys onto $Ti_3C_2T_x$ can induce interfacial electronic coupling, modify the d-band
65 structure, and optimize adsorption energetics, thereby enhancing catalytic activity.²¹ Density functional
66 theory (DFT) studies have demonstrated that dual-metal systems, such as Ni–Co, can synergistically
67 regulate the adsorption of ORR intermediates and lower the activation barriers. However, experimental
68 validation of these concepts under neutral-pH conditions relevant to MFCs remains limited.^{22,23}

69 In parallel, core–shell architectures combining metallic alloys and oxides have shown promise
70 in oxygen electrocatalysis.^{24,25} In these systems, the metallic core provides high electrical conductivity
71 and efficient charge transport, while the oxide shell offers abundant redox-active sites and favorable
72 adsorption properties.²⁴ The interplay between these components can create highly active and stable
73 catalytic interfaces.²⁵ Nevertheless, most studies have focused on alkaline or acidic environments, and
74 their applicability to neutral-pH MFC systems remains largely unexplored.

75 In this work, we address these challenges by designing a $(NiCoO_x@NiCo)/Ti_3C_2T_x$
76 heterostructure catalyst, in which NiCo alloy nanocores encapsulated within a thin oxide shell are
77 integrated with conductive $Ti_3C_2T_x$ sheets. This design is intended to modulate the local electronic
78 structure, optimize the adsorption energetics of oxygen intermediates, and facilitate charge transfer
79 under neutral conditions. By combining MXene surface chemistry with alloy-oxide core-shell
80 engineering and interfacial electronic coupling, this approach provides a platform to overcome the
81 intrinsic limitations of $Ti_3C_2T_x$. More broadly, it offers a rational framework for developing efficient



82 and durable platinum-group-metal-free ORR catalysts tailored for neutral-pH electrochemical systems
83 such as microbial fuel cells.

84 2. Experimental

85 2.1. Catalyst synthesis

86 **Synthesis of $Ti_3C_2T_x$ MXene.** The $Ti_3C_2T_x$ MXene was synthesized from Ti_3AlC_2 MAX phase
87 following a modified etching delamination procedure.²⁶ Briefly, 1 g of the Ti_3AlC_2 MAX powder
88 (99.99%, Carbon Ukraine) was gradually added (0.2 g min^{-1}) to a mixed etchant containing hydrofluoric
89 acid (HF, 40 wt.%, Sung Young Chemical Limited), hydrochloric acid (HCl, 37%, VWR Chemicals),
90 and deionized (DI) water in a volume ratio of 1:6:3 (total volume:10 mL). The mixture was stirred
91 continuously at 45 °C for 16 h.

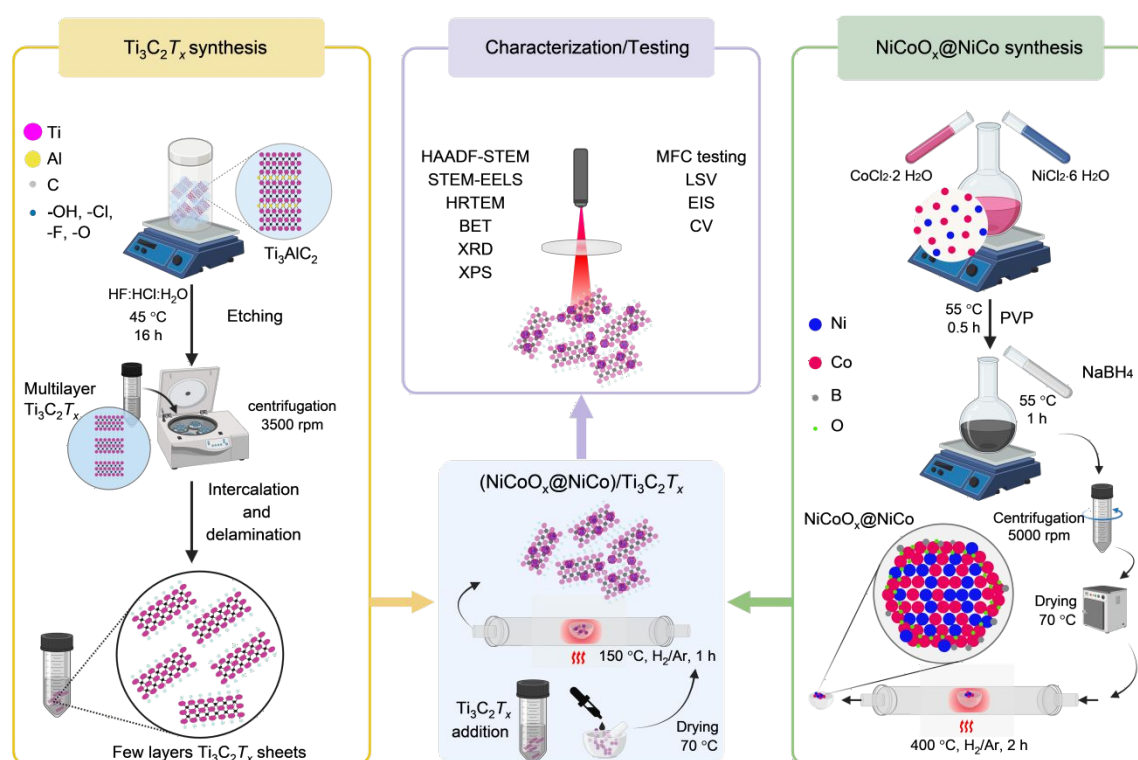
92 The obtained suspension was washed repeatedly with DI water (45 ml DI per wash; 3500 rpm;
93 5 min per cycle) until a stable dispersion was obtained. The washed product was then intercalated using
94 0.5 M lithium chloride (LiCl, 99%, Sigma-Aldrich) and subsequently delaminated via centrifugation to
95 yield few-layer $Ti_3C_2T_x$ sheets. The resulting colloidal suspension was under an argon atmosphere at 4
96 °C for further use.

97 **Synthesis of $NiCoO_x@NiCo$.** The $NiCoO_x@NiCo$ catalyst was synthesized via a combined
98 chemical reduction and thermal treatment approach.²⁷ First, equimolar quantities of Nickel(II) chloride
99 hexahydrate ($NiCl_2 \cdot 6H_2O$; 0.2025 mg) and Cobalt(II) chloride dihydrate ($CoCl_2 \cdot 2H_2O$; 0.1407 mg) were
100 separately dissolved in 10 mL of DI water. The Ni precursor was then added dropwise to the Co
101 precursor solution under continuous stirring, followed by further mixing for 10 min (320 rpm).
102 Separately, 0.5 g of polyvinylpyrrolidone (PVP, $(C_6H_9NO)_n$, MW 10000, Thermo Fisher Scientific) was
103 dissolved in 20 mL of DI water, and the solution was gradually added to the above mixture, which was
104 maintained at 55 °C with continuous stirring for 30 min. Subsequently, 0.4 mM sodium borohydride
105 ($NaBH_4$, 98%, Thermo Fisher Scientific) was added dropwise to initiate reduction, and the reaction was
106 allowed to proceed for 60 min. The resulting precipitate was collected, washed 6 times with DI water
107 and ethanol to remove residual reagents, and then vacuum-dried at 70 °C overnight. The dried product



108 was thermally reduced at 400 °C (heating rate: 5 °C min⁻¹) for 2 h under a 5% H₂ /Ar flow (100 mL
109 min⁻¹).

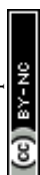
110 **Synthesis of (NiCoO_x@NiCo)/Ti₃C₂T_x composite.** To prepare the composite catalyst, 50 mg of
111 NiCoO_x@NiCo was dispersed in 10 mL of Ti₃C₂T_x colloidal suspension under continuous mixing. The
112 mixture was dried at 70 °C under an argon atmosphere, followed by mild thermal treatment at 150 °C
113 for 1 h under a 5% H₂ /Ar flow to promote interfacial integration between NiCoO_x@NiCo and Ti₃C₂T_x.
114 A schematic illustration of the synthesis procedure is presented in Figure 1.



116 Figure 1. Schematic overview of the synthesis procedures for Ti₃C₂T_x, NiCoO_x@NiCo, and the composite
117 (NiCoO_x@NiCo)/Ti₃C₂T_x catalyst, along with a summary of the physicochemical characterization techniques
118 employed for catalyst evaluation.

120 2.2. Catalyst characterization

121 Powder X-ray diffraction (XRD) patterns of the synthesized catalysts were recorded using a
122 Bruker D8 Advance diffractometer operating at 40 kV and 40 mA with Cu K α radiation ($\lambda = 1.5406 \text{ \AA}$),
123 over a 2θ range of 5-90° with a step size of 0.05°, and the resulting patterns were analyzed using
124 DIFFRAC.EVA software. The lattice strain induced by combining Ti₃C₂T_x and NiCoO_x@NiCo was
125 estimated by first computing the d spacing from the (111) plane of NiCoO_x@NiCo, using Bragg's law.



126 Next, the compressive lattice strain ($\varepsilon = \frac{d - d_0}{d_0}$) was evaluated based on the previously reported relative

View Article Online
DOI: 10.1039/C5TA03240K

127 change in interplanar spacing.^{28,29}

128 Quasi in situ X-ray photoelectron spectroscopy (XPS) measurements were performed using a
129 Kratos Axis Supra spectrometer equipped with a monochromatic Al K α source ($h\nu = 1486.6$ eV).
130 Measurements were conducted at 45 W under ultrahigh vacuum ($\sim 10^{-9}$ mbar). To minimize surface
131 oxidation, samples were transferred under inert conditions from the reduction environment to a glovebox
132 and mounted directly onto the XPS holder prior to analysis. Survey and high-resolution spectra were
133 collected using pass energies of 80 eV and 20 eV, respectively, over an analysis area of $300 \mu\text{m} \times 700$
134 μm . Samples were mounted in floating mode to minimize differential charging effects during XPS
135 measurements. Charge neutralization was applied for all samples. The binding energy scale was
136 calibrated using the main Ni 2p $_{3/2}$ peak corresponding to metallic Ni 0 , which was referenced at 852.6
137 eV. The peak deconvolution was carried out following the semi-empirical fitting approach reported.³⁰
138 where the fitting procedure was applied to quantify the photoelectron contributions corresponding to the
139 different chemical states present in the spectra.

140 Inductively coupled plasma optical emission spectroscopy (ICP-OES) was performed using
141 Varian, Inc./Agilent Model 7200-ES, to quantify the elemental composition of the catalysts. For
142 microwave-assisted digestion, approximately 0.03 g of catalyst was added to a mixture of concentrated
143 HCl (1 mL), concentrated HNO $_3$ (3 mL), and concentrated HF (1 mL). The mixture was then digested
144 under microwave irradiation with a 15 min ramp, and a 30 min hold at 493 K and 1000 W.

145 The Electron Paramagnetic Resonance (EPR) spectroscopy was conducted using a Bruker
146 ELEXSYS E500 EPR spectrometer operating in the X-band region, equipped with a high-sensitivity ER
147 4122 SHQ resonator. Measurements were performed at ambient temperature with a microwave
148 frequency of 9.3964 GHz and a sweep width of 8000 G. Field modulation was applied at 100 kHz with
149 a modulation amplitude of 5 G. The microwave power was set to 0.0474 W. Data acquisition and
150 processing were carried out using Bruker Xenon software.



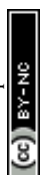
151 High-resolution transmission electron microscopy (HR-TEM), high-angle annular dark-field
152 scanning transmission electron microscopy (HAADF-STEM), and electron energy-loss spectroscopy
153 (EELS) were employed to investigate catalyst morphology and elemental distribution. STEM imaging
154 was performed using a Thermo Fisher Scientific Titan Themis Z microscope equipped with an HAADF
155 detector, operating at 300 kV and 0.05 nA. HAADF-STEM images were obtained at a convergence
156 angle of 20.9 mrad.

157 The nitrogen adsorption-desorption isotherms were measured at 77 K using a Micromeritics
158 ASAP 2040 analyzer to assess the surface characteristics of the catalyst samples. Specific surface area
159 was determined using the Brunauer-Emmett-Teller (BET) method. Scanning electron microscopy
160 (SEM) was used to examine biofilm attachment on the MFC anode. Imaging was performed using a
161 Thermo Fisher Scientific Quattro microscope.

162 2.3. Electrochemical testing

163 The electrocatalytic performance was evaluated using a standard three-electrode configuration
164 on a CH Instruments workstation equipped with a rotating disk electrode (RDE). A catalyst-coated
165 glassy carbon disk (3 mm diameter) served as the working electrode, with a graphite rod as the counter
166 electrode. Reference electrodes were selected according to the electrolyte: Ag/AgCl for ORR
167 measurements in phosphate-buffered saline (PBS, pH 7.4) and Hg/HgO for OER measurements in 0.5
168 M KOH (pH 13.2).

169 Prior to ORR measurements, the electrolyte was purged with N₂ for 30 min to remove dissolved
170 oxygen, followed by bubbling with O₂ for 1 h to achieve saturation. For OER testing, the electrolyte
171 was purged with N₂ for 30 min. Catalyst inks were prepared by dispersing 5 mg of
172 (NiCoO_x@NiCo)/Ti₃C₂T_x powder in a mixture of 960 μL isopropanol, 10 μL deionized water, and 30
173 μL Nafion solution, followed by sonication for 1 h. The ink was drop-cast onto the glassy carbon
174 electrode (loading: 0.42 mg cm⁻²) and dried under ambient conditions. Linear sweep voltammetry (LSV)
175 was conducted at scan rates of 10 mV s⁻¹ (ORR) and 1 mV s⁻¹ (OER) with a rotation speed of 1600
176 rpm. All potentials were converted to the reversible hydrogen electrode (RHE) scale using the Nernst



177 equation. Cyclic voltammetry (CV) measurements were performed under identical electrolyte
 178 conditions.

179 2.4. Microbial fuel cell testing

180 The ORR activity of the catalyst was evaluated in a single-chamber MFC equipped with an air-
 181 cathode and a total anodic volume of 100 mL (80 mL electrolyte and 20 mL headspace). A Nafion™
 182 117 membrane (NARA Cell-Tech Corporation, South Korea) separated the anode and cathode
 183 compartments to facilitate proton transport while minimizing oxygen crossover. The carbon paper (CP)
 184 and carbon cloth (CC) were pretreated by ultrasonication in acetone, rinsed with deionized water, and
 185 dried at 70 °C overnight. The cathode was prepared by depositing the catalyst onto CP (2.4 × 2.4 cm²),
 186 while pretreated CC served as the anode. Both electrodes were connected to stainless-steel current
 187 collectors.

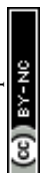
188 The anolyte was prepared from domestic wastewater collected from the KAUST treatment
 189 facility, supplemented with 20 mL of 1 M glucose to increase the organic content and stimulate
 190 microbial activity. The MFC was operated under ambient conditions, and cell voltage was continuously
 191 monitored. Polarization curves were obtained using linear sweep voltammetry (1 mV s⁻¹) after
 192 stabilization under open-circuit conditions. The internal resistance was determined from the slope of the
 193 linear region of the polarization curve.³¹

194 2.5. Electrochemical calculations

195 The electron transfer number was determined using the Koutecky-Levich (K–L) method, based
 196 on LSV measurements recorded at rotation speeds of 400, 900, 1600, and 2400 rpm.³² The reciprocal
 197 current density was plotted against the inverse square root of the rotation speed to obtain a linear
 198 relationship, from which *n* was calculated:

$$199 \frac{1}{j} = \frac{1}{j_k} + \frac{1}{j_l} = \frac{1}{j_k} + \frac{1}{0.62nFD^{2/3}\omega^{1/2}\mu^{-1/6}C_o} \quad (1),$$

200 where *j_k* and *j_l* denote the kinetic and diffusion-limited current densities, respectively;
 201 *n* is the number of electrons transferred; *F* is the Faraday constant (96,485 C mol⁻¹);



202 C^0 is the bulk concentration of O_2 in the electrolyte ($1.2 \times 10^{-3} \text{ mol L}^{-1}$); D is the O_2 diffusion coefficient
203 ($1.9 \times 10^{-5} \text{ cm}^2 \text{ s}^{-1}$); μ is the kinematic viscosity of the electrolyte; and ω is the angular rotation speed
204 of the disk ($\text{rad} \cdot \text{s}^{-1}$).

205 Electrochemical impedance spectroscopy (EIS) data were analyzed using ZView software.
206 Nyquist plots were fitted using an equivalent circuit model comprising solution resistance (R_s), charge-
207 transfer resistance (R_{ct}), and a constant-phase element (CPE), to account for non-ideal capacitive
208 behavior associated with surface roughness and porosity. The current (J) and power densities generated
209 by the MFC were calculated as follows:³¹

$$210 \quad J(\text{mA m}^{-2}) = \frac{I}{A_{\text{anode}}} \quad (2),$$

$$211 \quad P(\text{W m}^{-2}) = \frac{IV}{A_{\text{anode}}} \quad (3),$$

212 where I is the current, A_{anode} is the anode surface area, and V is the output voltage.

213 2.6. *Ab initio* calculations

214 Density functional theory (DFT) calculations were performed using the Vienna Ab initio
215 Simulation Package (VASP).³³ The projector-augmented wave (PAW) method was used to describe the
216 interaction between valence electrons and ionic cores, while exchange–correlation effects were treated
217 using the Perdew–Burke–Ernzerhof (PBE) functional within the generalized gradient approximation³⁴
218 Exchange-correlation effects were treated using the Perdew-Burke-Ernzerh within the generalized
219 gradient approximation.³⁵ A plane-wave cutoff energy of 520 eV was applied, and spin polarization was
220 included (ISPIN = 2).

221 A Monkhorst-Pack grid of $3 \times 3 \times 1$ was employed to sample the Brillouin zone.³⁶ Grimme's
222 DFT-D3 correction with Becke-Johnson damping (IVDW = 11) was employed to account for long-
223 range van der Waals interactions.³⁷ All structures were fully relaxed using the conjugate gradient
224 algorithm until the residual forces were below $0.02 \text{ eV} \text{ \AA}^{-1}$. Initial magnetic moments were assigned as



225 follows: Ti (2.0 μB), C (0.6 μB), Ni (2.0 μB), and Co (3.0 μB). Additional details regarding model
226 construction and reaction energetics are provided in the Supporting Information.

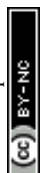
227 3. Results and discussions

228 3.1. Catalyst properties

229 The XRD analysis confirms the successful transformation of Ti_3AlC_2 to $\text{Ti}_3\text{C}_2\text{T}_x$, as evidenced
230 by the disappearance of the characteristic Al peak (014) at $\sim 39^\circ$, attributed to the MAX phase (Figure
231 2, green line).³⁸ Concurrently, a pronounced shift of the (002) peak toward lower 2θ values is observed
232 after etching (Figure 2, blue line), indicating an expansion of the interlayer spacing due to the removal
233 of Al layers and subsequent introduction of surface terminations and intercalated species.³⁹ Additional
234 reflections observed at $\sim 16^\circ$ and $\sim 28^\circ$ are assigned to the (004) and (006) planes of $\text{Ti}_3\text{C}_2\text{T}_x$, respectively,
235 confirming the preservation of the layered $\text{Ti}_3\text{C}_2\text{T}_x$ structure and long-range ordering along the c-axis
236 after delamination.³⁸ A weak reflection around $\sim 36^\circ$ is attributed to TiC, an impurity originating from
237 unreacted TiC during the synthesis of the MAX phase precursor.^{40,41}

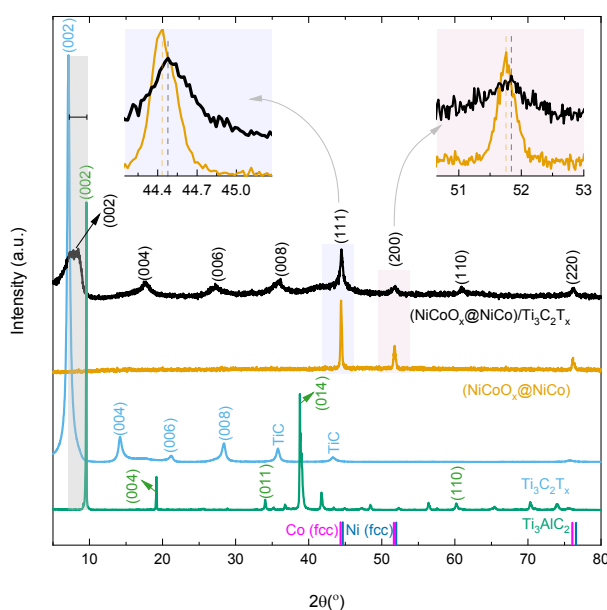
238 The $\text{NiCoO}_x@\text{NiCo}$ catalyst exhibited distinct diffraction peaks at 44.44° , 51.75° , and 76.18° ,
239 corresponding to the (111), (200), and (220) planes, respectively (PDF: 04-004-8490), as illustrated in
240 Figure 2 (orange line). These peaks appeared between the corresponding peaks of fcc-Ni and fcc-Co
241 (Figure 2, blue and magenta reference lines), confirming the formation of a NiCo alloy.⁴²⁻⁴⁵ Notably, no
242 discernible peaks associated with crystalline NiCoO_x are observed, suggesting that the oxide shell is
243 either amorphous, poorly crystalline, or confined to a thin surface layer, and therefore contributes
244 negligibly to the bulk diffraction signal.^{46,47}

245 For the $(\text{NiCoO}_x@\text{NiO})/\text{Ti}_3\text{C}_2\text{T}_x$ heterostructure (Figure 2, black line), the characteristic alloy
246 peaks are retained at slightly shifted positions (44.49° , 51.84° , and 76.28°), alongside the diffraction
247 features of $\text{Ti}_3\text{C}_2\text{T}_x$ shift to higher 2θ values, indicating a reduction in interlayer spacing. This behavior
248 is attributed to partial removal or rearrangement of surface terminations ($-\text{OH}$, $-\text{O}$, $-\text{F}$) and the
249 elimination of intercalated water during thermal treatment, leading to structural densification.⁴⁸ In
250 addition, the (002) peak of $\text{Ti}_3\text{C}_2\text{T}_x$ becomes broader and less intense after nanoparticle deposition,



251 indicating reduced crystallinity and partial structural disorder induced by nanoparticle anchoring and
 252 thermal processing.^{49,50}

253 A closer examination of the alloy reflections (insets in Figure 2) reveals slight positive shifts of
 254 $\sim 0.05^\circ$ and $\sim 0.09^\circ$ in the (111) and (200) planes, respectively, for the $(\text{NiCoO}_x@/\text{NiCo})/\text{Ti}_3\text{C}_2\text{T}_x$
 255 heterostructure compared to $\text{NiCoO}_x@/\text{NiCo}$. These shifts indicate lattice contraction, likely arising from
 256 interfacial electronic interactions between the NiCo alloy and the $\text{Ti}_3\text{C}_2\text{T}_x$ support, as well as possible
 257 charge-transfer effects involving surface terminations.⁵¹ Based on the shift in the (111) reflection, the
 258 compressive lattice strain (ϵ_{111}) was calculated to be -8.7×10^{-3} , confirming the presence of interface-
 259 induced compressive strain. This lattice distortion provides further evidence of strong coupling between
 260 the $\text{NiCoO}_x@/\text{NiCo}$ nanoparticles and the $\text{Ti}_3\text{C}_2\text{T}_x$ support⁵²



261
 262 Figure 2. XRD patterns of Ti_3AlC_2 (green line), $\text{Ti}_3\text{C}_2\text{T}_x$ (blue line), $\text{NiCoO}_x@/\text{NiCo}$ (orange line), and
 263 $(\text{NiCoO}_x@/\text{NiCo})/\text{Ti}_3\text{C}_2\text{T}_x$ (black line), along with reference patterns for fcc-Ni (blue vertical lines) and fcc-Co
 264 (magenta vertical lines). The right and left insets present magnified views of the (111) and (200) diffraction peaks,
 265 respectively, of the NiCo alloy in both $\text{NiCoO}_x@/\text{NiCo}$ and $(\text{NiCoO}_x@/\text{NiCo})/\text{Ti}_3\text{C}_2\text{T}_x$.
 266

267 The STEM imaging and elemental mapping of $\text{NiCoO}_x@/\text{NiCo}$ reveal a broad nanoparticle size
 268 distribution ranging from 8.5 nm to 115 nm and an average diameter of ~ 35 nm (Figure S1). The
 269 corresponding HAADF-STEM images (Figures 3a-c) show well-defined nanoparticles with a clear
 270 core-shell architecture, consisting of a metallic NiCo core encapsulated by an ultrathin (~ 4 nm) oxide



271 shell. Lattice-resolved imaging yields interplanar spacings of 0.216 nm and 0.188 nm, corresponding to
272 the (111) and (200) planes of the NiCo alloy, respectively (Figure 3c).^{24,53}

273 Fast Fourier Transform (FFT) pattern acquired from the core of the particle, displayed
274 diffraction spots indexed to the (111) and (200) planes of the metallic NiCo alloy, consistent with cubic
275 structure, $Fm\bar{3}m$ space group and lattice parameters $a = b = c = 3.54 \text{ \AA}$ and $\alpha = \beta = \gamma = 90^\circ$ (Figure 3d),
276 confirming its metallic nature. In contrast, FFT patterns obtained from the shell region (Figure 3e)
277 exhibit reflections consistent with a spinel NiCoO_x phase indexed to the $Fd\bar{3}m$ space group, with lattice
278 parameters $a = b = c = 8.065 \text{ \AA}$ and $\alpha = \beta = \gamma = 90^\circ$, verifying the formation of an oxide shell surrounding
279 the alloy core.

280 STEM–EELS elemental mapping of the $\text{NiCoO}_x@\text{NiCo}$ catalyst (Figures 3f, and 3k), further
281 resolves the spatial distribution of elements within individual particles. Ni and Co signals exhibit strong
282 spatial overlap, indicating homogeneous alloying within the core (Figures 3g, and 3h), while oxygen is
283 predominantly localized at the particle periphery, forming an O-rich shell (Figure 3i). The combined
284 elemental maps clearly delineate a NiCo-rich core enclosed by a NiCoO_x shell (Figure 3j). Line-scan
285 analysis confirms that both Ni and Co are present throughout the particle, with the core dominated by
286 metallic species and the shell enriched in oxygen-coordinated Ni/Co species (Figures 3k and 3l).

287 The HRTEM of a large area view of the $\text{NiCoO}_x@\text{NiCo}$ (Figure S2) demonstrates uniform
288 particle dispersion, while additional EELS analyses (Figures S3 and S4) reveal consistent elemental
289 distributions across multiple particles, confirming the reproducibility of the core–shell structure. Trace
290 amounts of boron (<2 at. %) are detected at the particle surface, likely originating from the NaBH_4 -
291 assisted reduction process.

292 The formation of a well-defined metal/oxide core–shell architecture is expected to generate
293 abundant interfacial sites between the conductive NiCo core and the redox-active NiCoO_x shell. Such
294 interfaces can facilitate efficient charge transport while providing active sites for oxygen adsorption and
295 transformation, thereby modulating the adsorption energetics of reaction intermediates through
296 interfacial electronic interactions.^{24,54}



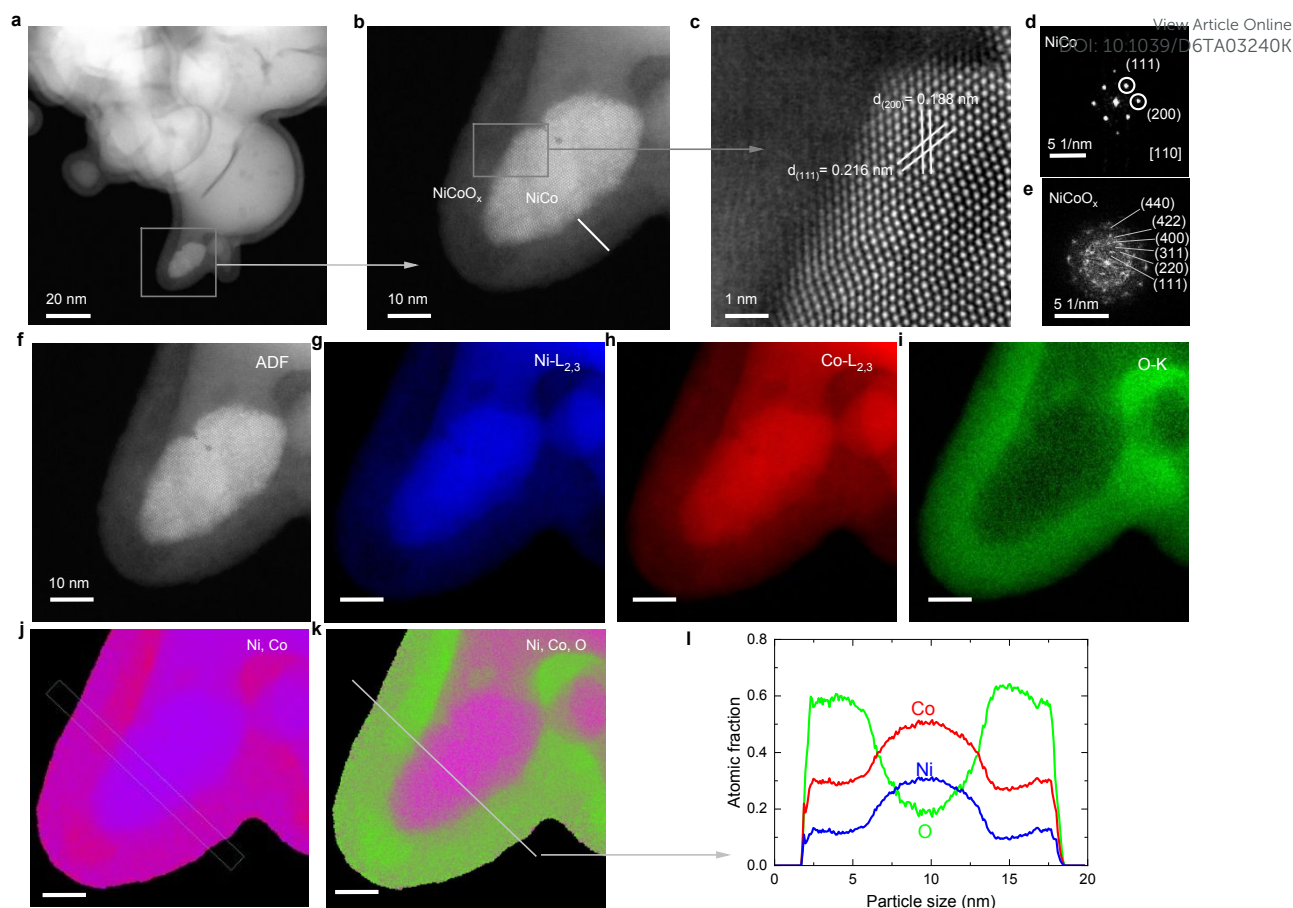


Figure 3. (a) HAADF-STEM image of the NiCoO_x@NiCo catalyst. (b, c) HR-STEM images of a type-1 grain. (d, e) FFTs derived from the corresponding HR-STEM images: (d) NiCo alloy core and (e) NiCoO_x shell. (f) ADF image of the type-1 grain. (g–i) EELS elemental maps of (g) Ni, (h) Co, (i) O, and (j) Overlay elemental mapping of Ni and Co. (k) Overlay elemental mapping of Ni, Co, and O, and (l) Corresponding atomic fraction profiles of Ni, Co, O obtained from the line scan indicated in (k). Abbreviations: HAADF-STEM, high-angle annular dark-field scanning transmission electron microscopy; HR-STEM, high-resolution STEM; FFT, fast Fourier transform; ADF, annular dark-field; EELS, electron energy loss spectroscopy.

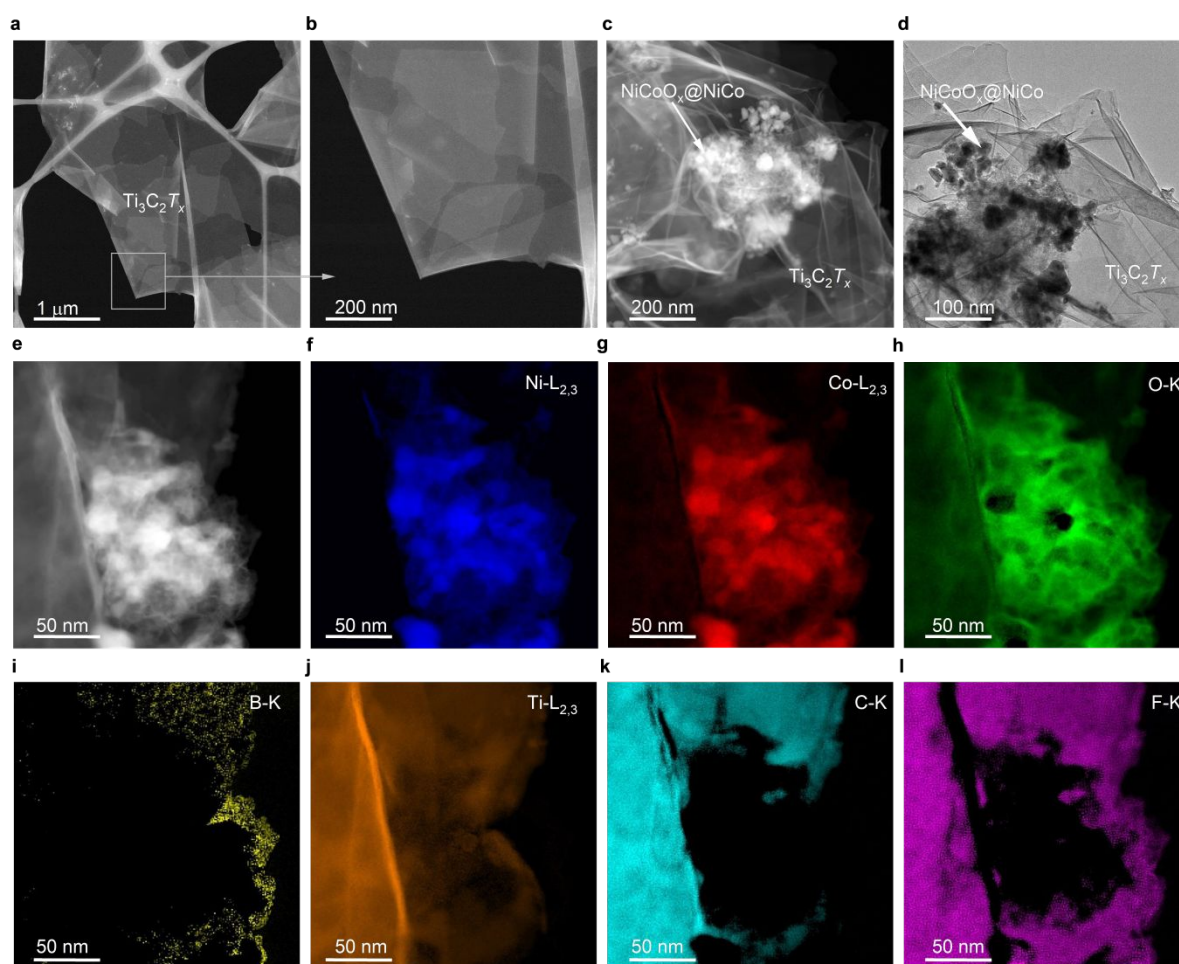
The HR-TEM analysis reveals that the Ti₃C₂T_x consists of a few-layered ultrathin sheets (Figures 4a-b), providing a suitable platform for nanoparticle anchoring. Upon integration, NiCoO_x@NiCo nanoparticles are uniformly distributed across the Ti₃C₂T_x surface, forming a well-defined heterostructure (Figures 4c-d). This morphology confirms the successful assembly of core-shell NiCoO_x@NiCo nanoparticles onto the MXene support.

STEM-EDX elemental mapping of pristine Ti₃C₂T_x (Figure S5) shows a homogeneous distribution of Ti, C, O, and F, consistent with the expected surface terminations (–O and –F) introduced during synthesis. In the (NiCoO_x@NiCo)/Ti₃C₂T_x heterostructure, STEM-EELS mapping (Figures 4e–l) further confirms the co-localization of Ti, C, O, and F with Ni and Co, indicating successful integration



315 of the nanoparticles without disrupting the MXene framework. This observation is consistent with the
 316 structural integrity inferred from XRD analysis (Figure 2).

317 Nitrogen adsorption–desorption measurements reveal a significant increase in surface area upon
 318 heterostructure formation. Pristine $\text{Ti}_3\text{C}_2\text{T}_x$ exhibits a low specific surface area ($\sim 3 \text{ m}^2 \text{ g}^{-1}$), in agreement
 319 with previous reports.⁵⁴ In contrast, the $(\text{NiCoO}_x@/\text{NiCo})/\text{Ti}_3\text{C}_2\text{T}_x$ composite displays a markedly higher
 320 surface area ($\sim 31 \text{ m}^2 \text{ g}^{-1}$), approaching that of the $\text{NiCoO}_x@/\text{NiCo}$ component ($\sim 32 \text{ m}^2 \text{ g}^{-1}$, Figure S6).
 321 This enhancement is primarily attributed to the incorporation of the nanoparticulate phase, which
 322 introduces additional accessible surface sites and modifies the composite's overall textural properties.



323
 324 Figure 4. (a, b) HAADF-STEM images of $\text{Ti}_3\text{C}_2\text{T}_x$. (c, d) HAADF-STEM and TEM images, respectively, of the
 325 $(\text{NiCoO}_x@/\text{NiCo})/\text{Ti}_3\text{C}_2\text{T}_x$ heterostructure. (e) ADF image of the $(\text{NiCoO}_x@/\text{NiCo})/\text{Ti}_3\text{C}_2\text{T}_x$ sample. (f–l)
 326 Corresponding EELS elemental maps for (f) B, (g) C, (h) O, (i) F, (j) Ti, (k) Co, and (l) Ni. Abbreviations: HAADF-
 327 STEM, high-angle annular dark-field scanning transmission electron microscopy; TEM, transmission electron
 328 microscopy; ADF, annular dark-field; EELS, electron energy loss spectroscopy.

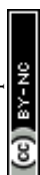
329



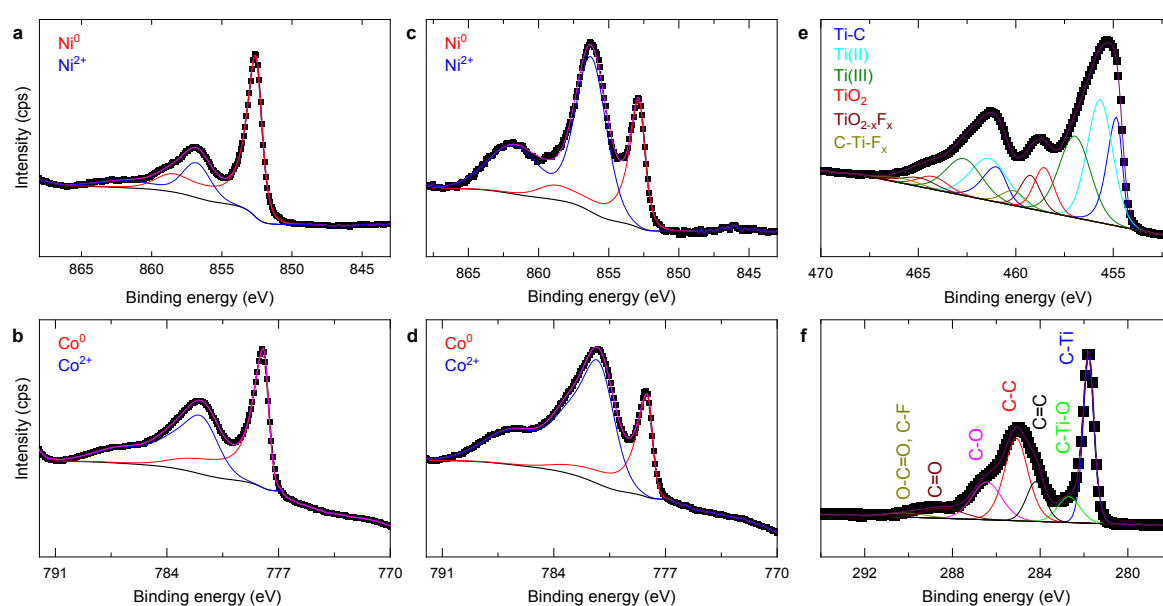
330 The surface chemical states of Ni, Co, and other elements (Figures 5 and S7) in the NiCo and
331 (NiCoO_x@NiCo)/Ti₃C₂T_x samples were analyzed by quasi in situ XPS after reduction at 400 °C under
332 an H₂/Ar atmosphere. For the NiCoO_x@NiCo sample, the Ni 2p spectrum (Figure 5a) exhibits a
333 dominant peak at ~852.6 eV corresponding to metallic Ni⁰^{30,55,56} together with an oxidized component
334 centered at ~856.2 eV and a pronounced shake-up satellite at ~861.7 eV, indicating that Ni
335 predominantly exists as Ni²⁺ species with a minor contribution from Ni³⁺.^{30,56} The Co 2p spectrum
336 (Figure 5b) shows a main Co 2p_{3/2} feature at ~781.8 eV accompanied by a satellite at ~786.8 eV,
337 indicating oxidized cobalt species mainly attributed to Co²⁺ with a small contribution of Co³⁺.^{30,56}
338 Meanwhile, the low-binding-energy peak at ~778.1 eV is assigned to metallic Co from the NiCo
339 alloy.^{30,56} The coexistence of metallic and oxidized Ni and Co species aligns with the STEM-EELS
340 observations, confirming a metallic NiCo core encapsulated by an NiCoO_x shell.

341 The (NiCoO_x@NiCo)/Ti₃C₂T_x heterostructure exhibits similar spectral features are observed,
342 with slight shifts in binding energy reflecting interfacial electronic interactions. The Ni 2p spectrum
343 (Figure 5c) indicates the coexistence of Ni⁰ and Ni²⁺/Ni³⁺ species, while the Co 2p spectrum (Figure 5d)
344 confirms that cobalt remains predominantly in the Co²⁺ state with minor Co³⁺ contribution. These results
345 demonstrate that the heterostructure retains a mixed metallic, oxidized character, indicative of strong
346 metal-oxide interfacial coupling. The Ti 2p (Figure 5e) and C 1s (Figure 5f) spectra confirm the
347 preservation of the Ti₃C₂T_x framework, with characteristic Ti–C bonding and partially oxidized Ti
348 species (Ti²⁺/Ti³⁺/Ti–O), consistent with surface terminations introduced during synthesis.

349 Quantitative XPS analysis (Table S1) reveals an increased Co/Ni surface ratio and a reduced
350 metallic fraction in the (NiCoO_x@NiCo)/Ti₃C₂T_x catalyst compared to NiCoO_x@NiCo, indicating a
351 higher proportion of oxidized surface species. This suggests that the Ti₃C₂T_x support promotes the
352 formation of oxidic interfacial species, consistent with NiCoO_x-like surface phases and in agreement
353 with HAADF-STEM-EELS observations (Figures 3 and 4). This finding demonstrates that the surface
354 of NiCoO_x@NiCo is dominated by Co²⁺ and Ni²⁺ states, with minor amounts of Co³⁺/Ni³⁺, indicating a
355 chemically and electronically heterogeneous surface. The mixed-valence chemical state is further
356 supported by EPR analysis (Figure S8). The NiCoO_x@NiCo sample exhibits a broad signal



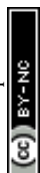
357 characteristic of strong magnetic exchange interactions, covering almost the entire range of the magnetic
 358 field sweep (around 7000 G), indicating coupling between transition metal centers via super exchange
 359 pathways (Co–O–Co and Co–O–Ni)^{57,58}. In contrast, the (NiCoO_x@NiCo)/Ti₃C₂T_x sample displays a
 360 well-defined Co²⁺ signal ($g \approx 2.155$), suggesting reduced magnetic coupling due to improved dispersion
 361 of active species on the Ti₃C₂T_x support.^{59,60} Compositional analysis of the samples using ICP (Table
 362 S2) confirmed the presence of both Ni and Co, with a Co/Ni ratio of 1.07 and 1.03 for NiCoO_x@NiCo
 363 and (NiCoO_x@NiCo)/Ti₃C₂T_x, respectively.



365 Figure 5. XPS spectra of the NiCoO_x@NiCo catalyst: (a) Ni 2p, (b) Co 2p, and of the (NiCoO_x@NiCo)/Ti₃C₂T_x
 366 catalyst: (c) Ni 2p, (d) Co 2p, (e) Ti 2p, (f) C 1s. Abbreviation: XPS, X-ray photoelectron spectroscopy.
 367
 368

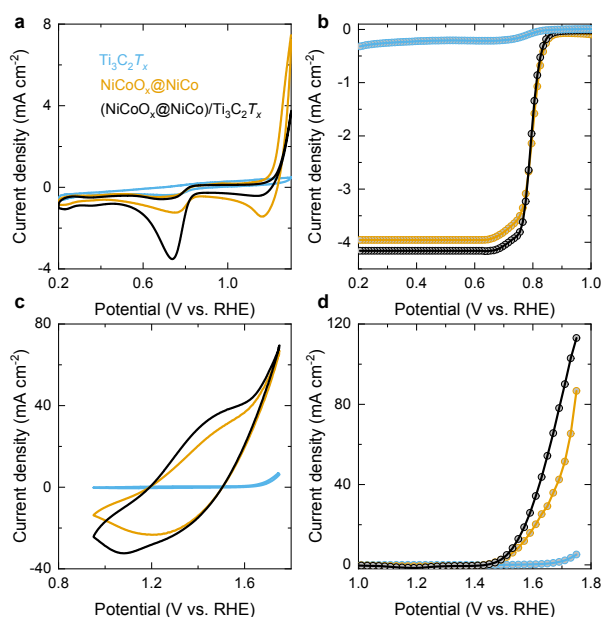
369 3.2. Electrochemical testing

370 The CV curves of all catalysts were recorded under an Ar atmosphere, showing similar
 371 capacitive behavior and reflecting comparable electrolyte environments (Figure S9). In contrast, under
 372 O₂-saturated conditions, the (NiCoO_x@NiCo)/Ti₃C₂T_x catalyst exhibits a markedly enhanced ORR
 373 response, delivering a higher cathodic peak current density (-3.5 mA cm^{-2} at 0.74 V) compared to
 374 NiCoO_x@NiCo (-1.24 mA cm^{-2} at 0.75 V) and Ti₃C₂T_x (-0.35 mA cm^{-2} at 0.70 V) (Figure 6a). This
 375 enhancement indicates improved catalytic activity and facilitates oxygen reduction kinetics.



376 Notably, the $(\text{NiCoO}_x@/\text{NiCo})/\text{Ti}_3\text{C}_2\text{T}_x$ achieves a higher peak current density than commercial
 377 10 wt% Pt/C under identical conditions, while exhibiting a comparable reduction potential ($\Delta E \approx 0.01$
 378 V) (Figure S10a). This suggests that the heterostructure provides competitive intrinsic activity, while
 379 the enhanced current response reflects improved charge transport and utilization of active sites.^{19,25}

380 LSV measurements at 1600 rpm further confirm the heterostructure's superior ORR
 381 performance. The $(\text{NiCoO}_x@/\text{NiCo})/\text{Ti}_3\text{C}_2\text{T}_x$ catalyst exhibits a half-wave potential ($E_{1/2}$) of 0.79 V and
 382 a limiting current density of -4.16 mA cm^{-2} , compared to 0.77 V and -3.98 mA cm^{-2} for
 383 $\text{NiCoO}_x@/\text{NiCo}$, and 0.80 V and -2.65 mA cm^{-2} for Pt/C (Figure 6b). All catalysts significantly
 384 outperform pristine $\text{Ti}_3\text{C}_2\text{T}_x$ (0.66 V and -0.26 mA cm^{-2}), highlighting the importance of heterostructure
 385 formation. The comparable half-wave potentials suggest similar intrinsic ORR kinetics, while the higher
 386 limiting current density of the heterostructure indicates enhanced mass transport and/or increased
 387 electrochemically accessible surface sites.



388
 389 Figure 6. Electrochemical performance of the catalysts (a, b) in the ORR: (a) CV and (b) LSV results, and in the (c,
 390 d) OER: (c) CV and (d) LSV results. Abbreviations: RHE, reversible hydrogen electrode; ORR, oxygen reduction
 391 reaction; OER, oxygen evolution reaction; CV, cyclic voltammetry; LSV, linear sweep voltammetry.

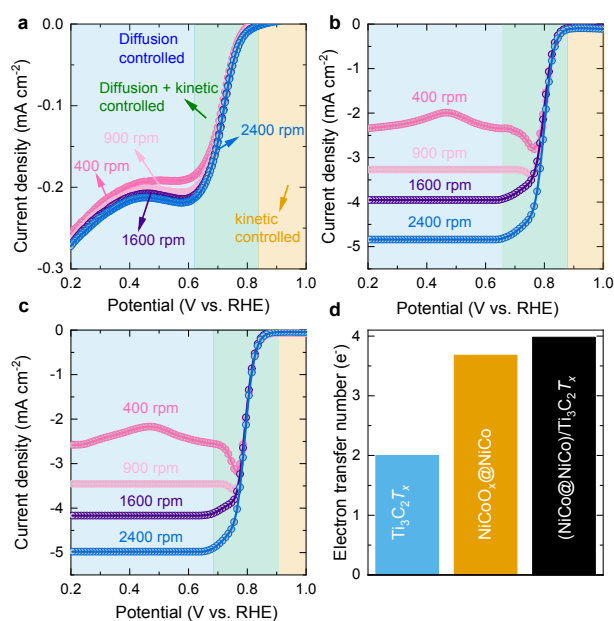
392
 393 To further evaluate the active surface characteristics, the electrochemically active surface area
 394 (ECSA) was estimated from the double-layer capacitance (C_{dl}) obtained via CV in the non-Faradaic
 395 region (0.0–0.10 V vs RHE) (Figures S11 and S12). The $(\text{NiCoO}_x@/\text{NiCo})/\text{Ti}_3\text{C}_2\text{T}_x$ catalyst exhibits the



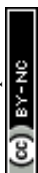
396 highest C_{dl} value ($375.2 \mu\text{F cm}^{-2}$), followed by $\text{NiCoO}_x@\text{NiCo}$ ($316.5 \mu\text{F cm}^{-2}$), Pt/C ($230.0 \mu\text{F cm}^{-2}$)
 397 and $\text{Ti}_3\text{C}_2\text{T}_x$ ($225.6 \mu\text{F cm}^{-2}$). The increased C_{dl} of the heterostructure indicates a larger
 398 electrochemically accessible surface area, thereby enhancing ORR activity.

399 The electron transfer number (n) per oxygen molecule during the ORR was determined using
 400 the K-L method, from LSV curves acquired during the rotating disk electrode measurements at varying
 401 rotation speeds (400, 900, 1600, and 2400 rpm) (Figures 7a-c). The increase in limiting current density
 402 with rotation speed reflects enhanced mass transport, arising from the thinning of the diffusion layer and
 403 improved O_2 flux to the catalyst surface.^{61,62} K-L plots derived from the LSV data exhibit good linearity,
 404 indicating first-order reaction kinetics with respect to dissolved oxygen and validating the reliability of
 405 the analysis. The electron transfer number was calculated from the slope of the K-L plots within the
 406 mixed kinetic-diffusion region (0.4–0.6 V vs RHE).⁶³

407 The $(\text{NiCoO}_x@\text{NiCo})/\text{Ti}_3\text{C}_2\text{T}_x$ catalyst displays an electron transfer number of ~ 3.98 ,
 408 approaching the ideal four-electron pathway for direct reduction of O_2 to OH^- . In comparison,
 409 $\text{NiCoO}_x@\text{NiCo}$ exhibits a lower value (~ 3.7), while pristine $\text{Ti}_3\text{C}_2\text{T}_x$ shows a value of ~ 2 , indicative of
 410 a two-electron pathway leading to peroxide intermediates (Figure 7d).⁶⁴



412
 413 Figure 7. LSV curves recorded at varying rotation speeds for the (a) $\text{Ti}_3\text{C}_2\text{T}_x$, (b) $\text{NiCoO}_x@\text{NiCo}$, and (c)
 414 $(\text{NiCoO}_x@\text{NiCo})/\text{Ti}_3\text{C}_2\text{T}_x$ catalysts. (d) Electron transfer numbers of the catalysts were calculated using the K-L



415 method. Abbreviations: LSV, linear sweep voltammetry; K-L, Koutecky–Levich; RHE, reversible hydrogen electrode.
416

Article Online
DOI: 10.1039/D6TA03240K

417 A 10 h chronoamperometric stability test under ORR conditions demonstrates that the
418 (NiCoO_x@NiCo)/Ti₃C₂T_x catalyst maintains >98% of its initial limiting current density, with no
419 observable change in onset potential (Figure S13). A slight negative shift in the half-wave potential
420 (0.79 to 0.74 V) is observed, indicating minor changes in intrinsic ORR kinetics while preserving overall
421 catalytic stability.

422 To further contextualize the catalytic behavior, the materials were also evaluated for OER. The
423 (NiCoO_x@NiCo)/Ti₃C₂T_x catalyst exhibits enhanced OER activity compared to its individual
424 components, delivering higher current densities at comparable overpotentials (Figures 6c-d). In contrast,
425 Ti₃C₂T_x alone shows negligible activity, confirming its limited intrinsic reactivity toward oxygen
426 electrochemistry and highlighting the critical role of the NiCoO_x@NiCo phase.

427 The EIS was employed to probe charge-transfer characteristics under ORR conditions. All
428 catalysts exhibit comparable solution resistance ($R_{\square} \approx 0.26\text{--}0.54 \Omega$), indicating similar electrolyte
429 environments (Figure 8a). The charge-transfer resistance (R_{ct}) follows the trend: Ti₃C₂T_x <
430 (NiCoO_x@NiCo)/Ti₃C₂T_x < NiCoO_x@NiCo. Despite a slightly higher R_{ct} than pristine Ti₃C₂T_x, the
431 heterostructure demonstrates improved overall electrochemical performance, suggesting that factors
432 beyond simple charge-transfer resistance, such as active site density and interfacial electronic effects,
433 govern ORR activity.^{65–67}

434 The Bode phase-angle plot (Figure 8c) of ORR provides further insight into frequency-
435 dependent charge-transfer behavior. Notably, the observed negative phase angles are typical in EIS
436 measurements of ORR/OER electrodes and arise from the capacitive nature of the electrode/electrolyte
437 interface, where charge is stored through double-layer charging, and the adsorption of surface reaction
438 intermediates.⁶⁸ In the plot, the high-frequency region (Figure 8c, pink region) corresponds to electron
439 transfer, while the low-frequency region (gray area) reflects interfacial mass transfer processes.⁶⁹ The
440 (NiCoO_x@NiCo)/Ti₃C₂T_x catalyst exhibits a lower phase angle (-55.23 degrees) at low frequencies (100-
441 103 Hz) and an intermediate phase angle (-15.97 degrees) at high frequencies (10³-10⁴ Hz), indicating
442 efficient mass transport and faster electron transport. The ORR catalytic activity of the catalysts can be

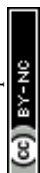


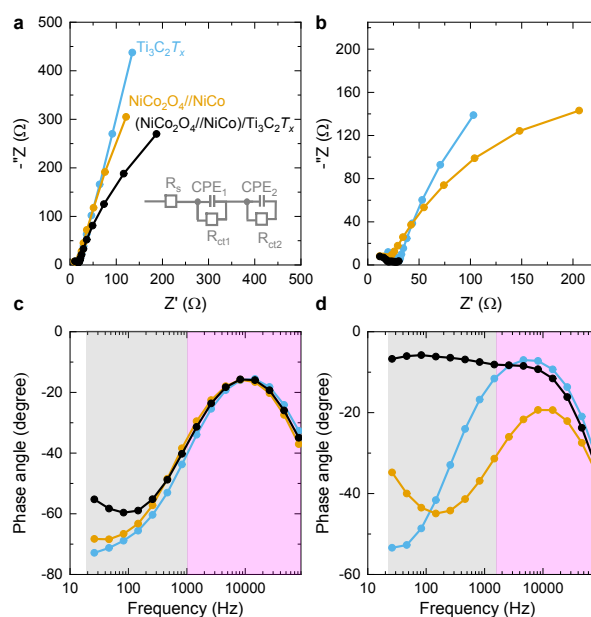
443 ranked as $\text{Ti}_3\text{C}_2\text{T}_x > (\text{NiCoO}_x@\text{NiCo})/\text{Ti}_3\text{C}_2\text{T}_x > \text{NiCoO}_x@\text{NiCo}$. This behavior is attributed to the high
444 electrical conductivity of $\text{Ti}_3\text{C}_2\text{T}_x$, which facilitates charge transport.⁷⁰

445 Furthermore, EIS measurements under OER conditions yielded comparable R_s values across all
446 three catalysts (2.4-3.9 Ω), indicating a uniform electrolyte environment. The $(\text{NiCoO}_x@\text{NiCo})/\text{Ti}_3\text{C}_2\text{T}_x$
447 catalyst exhibits the lowest R_{ct} value (16.7 Ω), indicating enhanced interfacial charge-transport. The
448 Bode phase angle plot shows a peak in the high-frequency region (10^3 - 10^4 Hz) (Figure 8d), associated
449 with the local electron transfer process.⁷¹ The $\text{NiCoO}_x@\text{NiCo}$ exhibited a higher phase angle (-19.33°)
450 in this region, suggesting slower electron transport. In contrast, $\text{Ti}_3\text{C}_2\text{T}_x$ exhibits the highest phase angle
451 (-7.23°), followed by $(\text{NiCoO}_x@\text{NiCo})/\text{Ti}_3\text{C}_2\text{T}_x$ (-9.28°), suggesting that the incorporation of $\text{Ti}_3\text{C}_2\text{T}_x$
452 facilitates faster electron transport.⁶⁷

453 Further analysis of EIS data for both OER and ORR using the Bode magnitude plot (Figure
454 S14) revealed reaction-dependent impedance behavior for OER. $(\text{NiCoO}_x@\text{NiCo})/\text{Ti}_3\text{C}_2\text{T}_x$ exhibits the
455 lowest impedance, indicating accelerated interfacial charge transfer and improved electron/ion transport
456 due to the coupling between conductive $\text{Ti}_3\text{C}_2\text{T}_x$ and $\text{NiCoO}_x@\text{NiCo}$ active sites. For ORR,
457 $\text{NiCoO}_x@\text{NiCo}$ exhibits the lowest impedance, suggesting that while $\text{Ti}_3\text{C}_2\text{T}_x$ improves the overall
458 conductivity and interfacial response, the ORR process may be more strongly governed by the intrinsic
459 $\text{NiCoO}_x@\text{NiCo}$ active phase.⁶⁸

460 The observed catalytic behavior arises from the synergistic interplay of multiple factors. XPS
461 analysis indicates a Co-enriched surface with mixed oxidation states ($\text{Co}^{2+}/\text{Co}^{3+}$) alongside metallic
462 NiCo, providing a redox-flexible environment for oxygen electrocatalysis. The coexistence of $\text{Ni}^{2+}/\text{Ni}^{3+}$
463 and $\text{Co}^{2+}/\text{Co}^{3+}$ species facilitates the adsorption and transformation of oxygenated intermediates, while
464 the metallic core ensures efficient electron transport. In combination with strong interfacial electronic
465 coupling with $\text{Ti}_3\text{C}_2\text{T}_x$, these features collectively enhance the catalytic performance.⁷²⁻⁷⁷





View Article Online
DOI: 10.1039/D6TA03240K

466

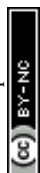
467 Figure 8. (a) EIS curve for the ORR; inset depicts the equivalent circuit model used to fit the EIS data. (b) EIS curve
468 for the OER. (c) Bode phase angle plot for the ORR. (d) Bode plot for the OER. Abbreviations: EIS, electrochemical
469 impedance spectroscopy; ORR, oxygen reduction reaction; OER, oxygen evolution reaction.

470

471 3.3. *Ab initio* calculations

472 Several Ti_3C_2 slabs: pristine (Figure S15a), O-functionalized (Figure S15b), OH-functionalized
473 (Figure S15c), and F-functionalized (Figure S15d), were prepared for the DFT simulation. To elucidate
474 the origin of the observed catalytic activity, NiCo-decorated Ti_3C_2T_x models were investigated, with Ni
475 and Co treated as active sites (Figure S16). It is important to note that the DFT model employs a
476 simplified Ni–Co double-atom catalyst (DAC) configuration containing one Ni and one Co atom. This
477 model is designed to probe local active-site chemistry and intrinsic catalytic roles, rather than to
478 reproduce the exact experimental Ni ratio. Therefore, the calculations provide mechanistic insight into
479 site-specific activity, independent of the macroscopic elemental composition.

480 Figures 9 and S17 illustrate the thermodynamic reaction profiles for the ORR and OER,
481 respectively. Notably, ORR and OER are reverse electrochemical processes that proceed through the
482 same adsorbed intermediates ($^*\text{OOH}$, $^*\text{O}$, and $^*\text{OH}$), but in opposite directions. Consequently, the
483 catalytic performance in both reactions is governed by the ability of the catalyst to balance the adsorption
484 energies of the shared intermediates.



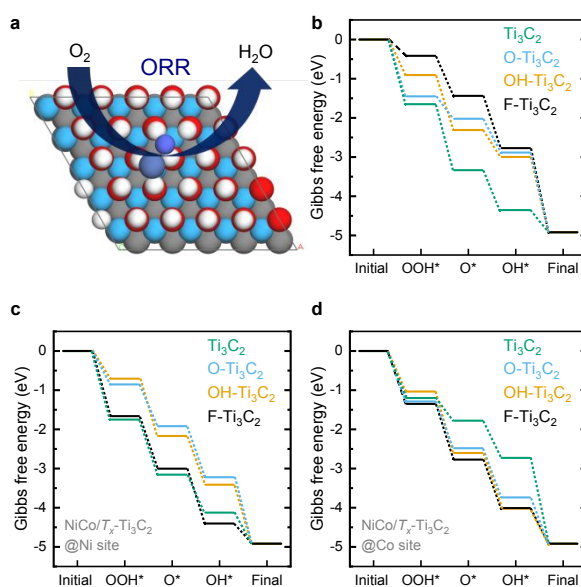
485 Bare and functionalized Ti_3C_2 surfaces exhibit strong overbinding of key intermediates ($^*\text{O}$ and
486 $^*\text{OH}$), leading to excessive exergonic adsorption and large uphill steps ($\Delta G > 2.0$ eV). This imbalance
487 results in sluggish ORR kinetics and prohibitively high OER overpotentials, aligning with previous
488 reports indicating that $\text{Ti}_3\text{C}_2\text{T}_x$ is intrinsically a poor ORR/OER catalyst due to its inability to balance
489 adsorption–desorption energetics.⁷⁸ Although bare and functionalized MXenes (Ti_3C_2 , O- Ti_3C_2 , OH-
490 Ti_3C_2 , and F- Ti_3C_2) exhibit highly exergonic ORR energetics (Figure 9b), supporting their
491 thermodynamic feasibility. The adsorption energies of key intermediates remained excessively large.
492 For instance, $^*\text{OOH}$ adsorption energies reached -1.65 eV for Ti_3C_2 , -1.45 eV for O- Ti_3C_2 , and -1.40
493 eV for OH- Ti_3C_2 , while the $^*\text{OH}$ adsorption energy for F- Ti_3C_2 was as low as -2.15 eV (Table S3). Such
494 low potential reflects severe overbinding, particularly of $^*\text{OH}$, which may poison the active sites and
495 suppress catalytic turnover. Further, the OER profiles (Figure S17a) exhibited prohibitively large uphill
496 steps. Notably, the $^*\text{OH} \rightarrow ^*\text{O}$ transition represents the most endergonic step, with ΔG values of 2.04
497 eV for O- Ti_3C_2 , 2.15 eV for Ti_3C_2 , and 1.92 eV for OH- Ti_3C_2 . These substantial energy barriers
498 correspond to high theoretical overpotentials (>0.9 V), thereby rendering these surfaces ineffective for
499 the OER. This analysis confirms that bare Ti_3C_2 , despite its strong oxygen affinity, is an intrinsically
500 poor ORR and OER electrocatalyst owing to its inability to balance the energetics of adsorption and
501 desorption of intermediates.⁶⁴

502 Upon NiCo incorporation, the thermodynamic profiles are significantly improved. Structural
503 optimization reveals stable adsorption of $^*\text{OOH}$, $^*\text{O}$, and $^*\text{OH}$ intermediates across both Ni and Co
504 sites, with $^*\text{OOH}$ frequently relaxing into bridge configurations, indicating cooperative interaction
505 between the two metals (Figure S17). To distinguish their catalytic roles, two configurations were
506 analyzed: (i) NiCo@Ni, considering Ni as an active site, and (ii) NiCo@Co, considering Co as an active
507 site. The results reveal a clear functional asymmetry: In the Ni-centered ORR pathway (Figure 9c), Ni
508 sites reduced $^*\text{OH}$ binding energies to moderate values (e.g., -0.80 to -1.70 eV), in contrast to the
509 excessively high adsorption energies observed for bare Ti_3C_2 . In parallel, the initial O_2 activation step
510 ($+\text{O}_2 \rightarrow ^*\text{OOH}$) became less exergonic, with ΔG ranging from -0.85 to -1.75 eV. In the Co-centered



511 ORR pathway (Figure 9d), Co sites exhibit more balanced adsorption of *O and *OH intermediates,
 512 resulting in smoother free-energy profiles and lower thermodynamic barriers (Table S3).

513 Notably, the Co-centered ORR pathway exhibits reaction steps closer to the ideal
 514 thermodynamic value (~ -1.23 eV per step), indicating superior catalytic efficiency for oxygen
 515 intermediate transformation. Similarly, for OER, the NiCo@Co configuration significantly lowers the
 516 rate-limiting step (*O \rightarrow *OOH, $\Delta G \approx +1.03$ eV), corresponding to a low theoretical overpotential
 517 (~ 0.20 V). These results demonstrate that Ni and Co cooperatively connect ORR and OER pathways
 518 through complementary roles: Ni promotes ORR initiation via *OOH stabilization, while Co governs
 519 the energetics of *O and *OH intermediates, which are critical for both ORR progression and OER rate-
 520 determining steps. This synergy enables a balanced adsorption–desorption landscape, which is essential
 521 for efficient bifunctional catalysis. Importantly, this DFT-derived mechanism is fully consistent with
 522 experimental observations. XPS (Figure 5) and STEM analysis (Figure 3) reveal a Co-enriched surface
 523 composition, while the DFT results identify Co as the more active site for oxygen intermediate binding.



524
 525 Figure 9. Representative geometry of the catalyst system. The red, white, gray, blue, and purple spheres represent
 526 oxygen, hydrogen, carbon, titanium, and NiCo, respectively. (b) ORR free energy profiles for bare and functionalized
 527 MXenes (Ti₃C₂, O-Ti₃C₂, OH-Ti₃C₂, F-Ti₃C₂). (c, d) Free energy profiles of NiCo-decorated Ti₃C₂-based MXene with
 528 various terminations: (c) NiCo@Ni and (d) NiCo@Co systems.

529
 530

531 3.4. Bioelectrochemical tests

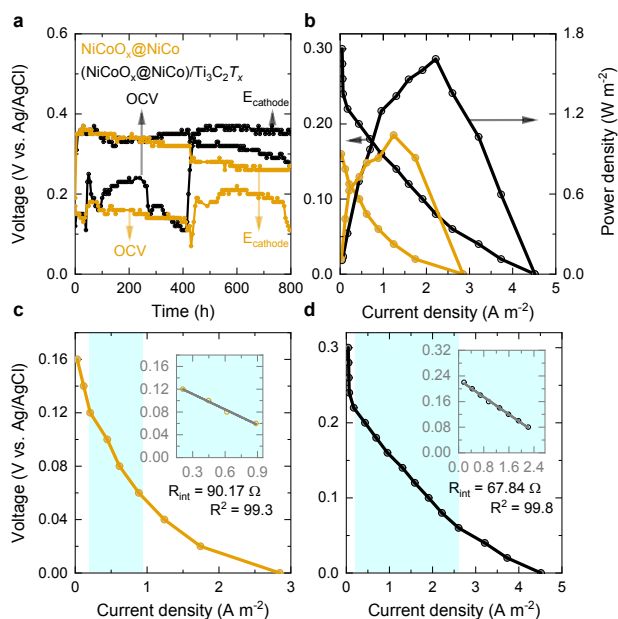


532 The bioelectrochemical performance of the catalysts was evaluated in air-cathode MFCs over
533 an extended 800 h operating period. The temporal evolution of anode potential (Figure S18) and open-
534 circuit voltage (OCV) (Figure 10a) shows an inverse relationship, where a decrease in anode potential
535 corresponds to an increase in OCV, reflecting electron accumulation at the anode. A transient drop in
536 OCV at ~400 h coincides with electrolyte replacement, after which both OCV and electrode potentials
537 stabilize over subsequent operation cycles.

538 Following stabilization, polarization measurements were conducted. The
539 (NiCoO_x@NiCo)/Ti₃C₂T_x cathode achieves a higher operating potential (360 mV) compared to
540 NiCoO_x@NiCo (280 mV) (Figure 10a). Correspondingly, the heterostructure delivers an enhanced
541 current density (4.5 A m⁻²) and maximum power density (1.6 W m⁻²), exceeding those of
542 NiCoO_x@NiCo (2.9 A m⁻² and 0.9 W m⁻², respectively) (Figure 10b). The internal resistance, estimated
543 from the slope of the polarization curve, is lower for the (NiCoO_x@NiCo)/Ti₃C₂T_x based MFC (67.84
544 Ω) than for NiCoO_x@NiCo (90.17 Ω) (Figure 10c,d), indicating improved charge transport and reduced
545 ohmic losses.⁷⁷ Collectively, these results demonstrate the superior cathodic performance of the
546 heterostructure relative to the single-phase catalyst and place it among competitive platinum-group-
547 metal-free systems.^{79–82}

548 The SEM analysis of the used anode reveals comparable biofilm coverage for both systems
549 (Figure S19), indicating that the observed performance differences originate primarily from cathode
550 properties rather than biological variability. The enhanced activity of the (NiCoO_x@NiCo)/Ti₃C₂T_x
551 catalyst can be attributed to the synergistic interplay between its components. Mixed-valence Co species
552 (Co²⁺/Co³⁺) provide redox-active sites for oxygen intermediate adsorption, while Ni contributes to
553 electronic modulation and stabilization of reaction intermediates. In parallel, the conductive
554 Ti₃C₂T_x scaffold facilitates efficient electron transport and promotes strong interfacial coupling with the
555 NiCoO_x@NiCo phase. This integrated design enables improved ORR kinetics and charge-transfer
556 efficiency under neutral conditions, highlighting the potential of MXene-based heterostructures as
557 effective cathode catalysts for sustainable energy generation in microbial fuel cells.





View Article Online
DOI: 10.1039/D6TA03240K

558

559 Figure 10. (a) Long-term MFC operation over 800 h. (b) Polarization and power density curves of MFC incorporating
 560 the $\text{NiCoO}_x@/\text{NiCo}$ and $(\text{NiCoO}_x@/\text{NiCo})/\text{Ti}_3\text{C}_2\text{T}_x$ cathodes. (c, d) R_{int} of MFC incorporating the $\text{NiCoO}_x@/\text{NiCo}$ and
 561 $(\text{NiCoO}_x@/\text{NiCo})/\text{Ti}_3\text{C}_2\text{T}_x$ cathodes, respectively. Abbreviations: R_{int} , internal resistance; MFC, microbial fuel cell;
 562 OCV, open-circuit voltage.
 563



564 4. Conclusions

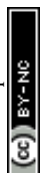
565 This study presents a rationally engineered (NiCoO_x@NiCo)/Ti₃C₂T_x heterostructure catalyst
566 for ORR under neutral-pH conditions, directly addressing the critical requirements of MFCs. Compared
567 with pristine Ti₃C₂T_x, the heterostructure exhibits markedly enhanced ORR activity, characterized by a
568 higher limiting current density and reduced overpotential, indicative of accelerated reaction kinetics and
569 a more favorable oxygen reduction pathway in neutral electrolyte.

570 Comprehensive structural and spectroscopic analyses unequivocally confirm the formation of a
571 well-defined NiCoO_x@NiCo core-shell architecture uniformly anchored on conductive Ti₃C₂T_x sheets.
572 The synergistic coexistence of metallic NiCo cores and oxidized NiCoO_x shells, coupled with strong
573 interfacial electronic interactions with the Ti₃C₂T_x support, facilitates rapid charge transport, maximizes
574 active-site exposure, and optimizes the adsorption energetics of oxygen intermediates. Complementary
575 DFT calculations provide mechanistic insight, revealing a distinct functional synergy between Ni and
576 Co active centers: Ni preferentially stabilizes *OOH intermediates, while Co regulates *O and *OH
577 binding. This cooperative interplay effectively modulates the local electronic structure of Ti₃C₂T_x,
578 alleviates its intrinsic overbinding limitations, and establishes a balanced adsorption-desorption
579 landscape essential for efficient ORR under neutral conditions.

580 In the real air-cathode MFC, the (NiCoO_x@NiCo)/Ti₃C₂T_x electrode achieves a high current
581 density of 4.5 A m⁻² and a peak power density exceeding 1.6 W m⁻², outperforming both pristine
582 Ti₃C₂T_x and benchmark NiCo-based catalysts. These results not only demonstrate the practical viability
583 of the proposed catalyst in wastewater-driven bioelectrochemical systems, but also highlight the
584 effectiveness of integrating Ti₃C₂T_x conductivity, core-shell chemistry, and interfacial electronic tuning
585 as a unified strategy for advancing neutral-pH electrocatalysis.

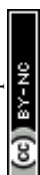
586 Acknowledgments

587 This research was supported by King Abdullah University of Science and Technology (KAUST,
588 BAS/1/1403). The authors thank Dr. Ananda Rao Hari for providing wastewater from the KAUST
589 wastewater treatment facility.



590 **References**View Article Online
DOI: 10.1039/D6TA03240K

- 591 1 Y. Zhao, D. P. Adiyeri Saseendran, C. Huang, C. A. Triana, W. R. Marks, H. Chen, H. Zhao
592 and G. R. Patzke, *Chem. Rev.*, 2023, **123**, 6257–6358.
- 593 2 Z. F. Huang, J. Wang, Y. Peng, C. Y. Jung, A. Fisher and X. Wang, *Adv. Energy Mater.*, 2017,
594 **7**, 1700544.
- 595 3 M. David, C. Ocampo-Martínez and R. Sánchez-Peña, *J. Energy Storage*, 2019, **23**, 392–403.
- 596 4 N. Du, C. Roy, R. Peach, M. Turnbull, S. Thiele and C. Bock, *Chem. Rev.*, 2022, **122**, 11830–
597 11895.
- 598 5 J. Pak, W. Chang, C. H. Kwon and J. Cho, *Adv. Funct. Mater.*, 2025, **35**, 2415933.
- 599 6 S. Gupta, A. Patro, Y. Mittal, S. Dwivedi, P. Saket, R. Panja, T. Saeed, F. Martínez and A. K.
600 Yadav, *Sci. Total Environ.*, 2023, **879**, 162757.
- 601 7 M. A. Aminudin, S. K. Kamarudin, B. H. Lim, E. H. Majilan, M. S. Masdar and N. Shaari, *Int.*
602 *J. Hydrog. Energy*, 2023, **48**, 4371–4388.
- 603 8 Q. Wang, S. Kaushik, X. Xiao and Q. Xu, *Chem. Soc. Rev.*, 2023, **52**, 6139–6190.
- 604 9 B. E. Logan, *Appl. Microbiol. Biotechnol.*, 2010, **85**, 1665–1671.
- 605 10 J. V. Boas, V. B. Oliveira, M. Simões and A. M. F. R. Pinto, *J. Environ. Manag.*, 2022, **307**,
606 114525.
- 607 11 M. D. Bhatt and J. Y. Lee, *Energ Fuel.*, 2020, **34**, 6634–6695.
- 608 12 X. Tian, X. F. Lu, B. Y. Xia and X. W. (David) Lou, *Joule*, 2020, **4**, 45–68.
- 609 13 X. X. Wang, J. Sokolowski, H. Liu and G. Wu, *Chinese J. Catal.*, 2020, **41**, 739–755.
- 610 14 T. Toda, H. Igarashi and M. Watanabe, *J. Electrochem. Soc.*, 1998, **145**, 4185–4188.
- 611 15 X. Chia and M. Pumera, *Nat. Catal.*, 2018, **1**, 909–921.
- 612 16 F. R. Fan, R. Wang, H. Zhang and W. Wu, *Chem. Soc. Rev.*, 2021, **50**, 10983–11031.
- 613 17 Q. Fu, J. Han, X. Wang, P. Xu, T. Yao, J. Zhong, W. Zhong, S. Liu, T. Gao, Z. Zhang, L. Xu
614 and B. Song, *Adv. Mater.*, 2021, **33**, 1–24.
- 615 18 Y. Wang, M. Zhang, Y. Liu, Z. Zheng, B. Liu, M. Chen, G. Guan and K. Yan, *Adv. Sci.*, 2023,
616 **10**, 1–28.
- 617 19 A. Thakur, Y. Zhang, Y. Gogotsi and B. Anasori, *MRS Energy Sustain.*, 2025, 1–13.
- 618 20 B. Anasori and Y. Gogotsi, *Graphene 2D Mater.*, 2022, **7**, 75–79.
- 619 21 X. Wang, D. Luo, J. Wang, Z. Sun, G. Cui, Y. Chen, T. Wang, L. Zheng, Y. Zhao, L. Shui, G.
620 Zhou, K. Kempa, Y. Zhang and Z. Chen, *Angew. Chem. Int. Ed.*, 2021, **60**, 2371–2378.
- 621 22 M. Hu, L. Chen, Y. Wang, J. Dai, Y. Bi, Y. Li, J. Zhao, G. Li, L. Wang, A. Meng and Z. Li, *J.*
622 *Chem. Eng.*, 2025, **513**, 162785.
- 623 23 Y. Guan, Y. Cong, R. Zhao, K. Li, X. Li, H. Zhu, Q. Zhang, Z. Dong and N. Yang, *Small*,
624 2023, **19**, 2301276.
- 625 24 H. Xu, Z. X. Shi, Y. X. Tong and G. R. Li, *Adv. Mater.*, 2018, **30**, 1705442.
- 626 25 C. Chen, H. Su, L. N. Lu, Y. S. Hong, Y. Chen, K. Xiao, T. Ouyang, Y. Qin and Z. Q. Liu,
627 *Chem. Eng. J.*, 2021, **408**, 127814.
- 628 26 P. D. Kolubah, H. O. Mohamed, A. R. Hari, Y. Ping, M. Ben Hassine, P. Dally, M. Obaid, X.
629 Xu, J. K. El-Demellawi, P. E. Saikaly, M. Lanza, N. Ghaffour and P. Castaño, *Small*, 2024,
630 2406223.
- 631 27 B. E. Logan, *Appl. Microbiol. Biotechnol.*, 2010, **85**, 1665–1671.
- 632 28 J. Wu, P. Li, Y. T. Pan, S. Warren, X. Yin and H. Yang, *Chem. Soc. Rev.*, 2012, **41**, 8066–
633 8074.
- 634 29 C. Wu, H. Li, H. He, Y. Song, C. Bi, W. Du and H. Xia, *ACS Appl. Mater. Interfaces*, 2019,
635 **11**, 46902–46911.
- 636 30 M. C. Biesinger, B. P. Payne, A. P. Grosvenor, L. W. M. Lau, A. R. Gerson and R. S. C.
637 Smart, *Appl. Surf. Sci.*, 2011, **257**, 2717–2730.
- 638 31 B. E. Logan, B. Hamelers, R. Rozendal, U. Shroder, J. Kelle, S. Freguia, P. Aelterman, W.
639 Verstraete and K. Rabaey, *Environ. Sci. Technol.*, 2006, **40**, 5181–5192.
- 640 32 R. Zhou, Y. Zheng, M. Jaroniec and S. Z. Qiao, *ACS Catal.*, 2016, **6**, 4720–4728.
- 641 33 G. Kresse and J. Furthmüller, *Phys. Rev. B*, 1996, **54**, 11169.
- 642 34 P. E. Blöchl, *Phys. Rev. B*, 1994, **50**, 17953.



- 643 35 J. P. Perdew, K. Burke and M. Ernzerhof, *Phys. Rev. Lett.*, 1996, **77**, 3865.
- 644 36 H. J. Monkhorst and J. D. Pack, *Phys. Rev. B*, 1976, **13**, 5188.
- 645 37 S. Grimme, J. Antony, S. Ehrlich and H. Krieg, *J. Chem. Phys.*,
646 DOI:10.1063/1.3382344/926936.
- 647 38 K. R. G. Lim, M. Shekhirev, B. C. Wyatt, B. Anasori, Y. Gogotsi and Z. W. Seh, *Nat. Synth.*,
648 2022, **1**, 601–614.
- 649 39 A. Thakur, N. Chandran B.S., K. Davidson, A. Bedford, H. Fang, Y. Im, V. Kanduri, B. C.
650 Wyatt, S. K. Nemani, V. Poliukhova, R. Kumar, Z. Fakhraai and B. Anasori, *Small Methods*,
651 2023, **7**, 2300030.
- 652 40 X. Wang, X. Fan, M. Li, W. Zhu, J. Xue, F. Ye and L. Cheng, *Ceram. Int.*, 2021, **47**, 13628–
653 13634.
- 654 41 M. Downes, C. E. Shuck, B. McBride, J. Busa and Y. Gogotsi, *Nat. Protoc.*, 2024, **19**, 1807–
655 1834.
- 656 42 B. Zhang, X. Zhang, Y. Wei, L. Xia, C. Pi, H. Song, Y. Zheng, B. Gao, J. Fu and P. K. Chu, *J.*
657 *Alloy. Compd.*, 2019, **797**, 1216–1223.
- 658 43 S. Huang, W. Zhang, Q. Chen, S. Zhou, L. Sun, L. Sha, G. Zhuang, P. Wang and X. Han,
659 *Chem. Eur. J.*, 2023, **29**, e202300321.
- 660 44 L. Wang, B. Wen, X. Bai, C. Liu and H. Yang, *ACS Appl. Nano Mater.*, 2019, **2**, 7827–7838.
- 661 45 M. Cheng, M. Wen, S. Zhou, Q. Wu and B. Sun, *Inorg. Chem.*, 2012, **51**, 1495–1500.
- 662 46 J. Fan, H. Zheng, A. Chen, L. Gu, X. Xie, J. Fan and Z. Ding, *Chem. Eng. J.*, 2023, **476**,
663 146638.
- 664 47 X. Yan, K. Li, L. Lyu, F. Song, J. He, D. Niu, L. Liu, X. Hu and X. Chen, *ACS Appl. Mater.*
665 *Interfaces*, 2016, **8**, 3208–3214.
- 666 48 J. Zhang, K. A. S. Usman, M. A. N. Judicpa, D. Hegh, P. A. Lynch and J. M. Razal, *Small*
667 *Methods*, 2023, **7**, 2201527.
- 668 49 W. Hou, Y. Sun, Y. Zhang, T. Wang, L. Wu, Y. Du and W. Zhong, *J. Alloy. Compd.*, 2021,
669 **859**, 157797.
- 670 50 T. Wang, K. Yao, Y. Hua, E. G. Shankar, R. Shanthappa and J. S. Yu, *Chem. Eng. J.*, 2023,
671 **457**, 141363.
- 672 51 P. P. Waghmaitar, S. B. Alex, L. Vazhayal, S. Kad, R. R. Urkude, B. Ghosh and S. K. Haram,
673 *ACS Appl. Energy Mater.*, 2025, **8**, 14519–14529.
- 674 52 B. Hu, Y. Xie, Y. Yang, J. Meng, J. Cai, C. Chen, D. Yu and X. Zhou, *Dalt. Trans.*, 2023, **52**,
675 12002–12009.
- 676 53 Z. Q. Liu, K. Xiao, Q. Z. Xu, N. Li, Y. Z. Su, H. J. Wang and S. Chen, *RSC Adv.*, 2013, **3**,
677 4372–4380.
- 678 54 M. X. Jin, Y. L. Pu, Z. J. Wang, Z. Zhang, L. Zhang, A. J. Wang and J. J. Feng, *ACS Appl.*
679 *Energy Mater.*, 2019, **2**, 4188–4194.
- 680 55 A. P. Grosvenor, M. C. Biesinger, R. S. C. Smart and N. S. McIntyre, *Surf. Sci.*, 2006, **600**,
681 1771–1779.
- 682 56 B. Laïk, M. Richet, N. Emery, S. Bach, L. Perrière, Y. Cotrebil, V. Russier, I. Guillot and P.
683 Dubot, *ACS Omega*, 2024, **9**, 40707–40722.
- 684 57 P. W. ANDERSON, *Phys. Rev.*, 1950, **79**, 350–355.
- 685 58 J. B. Goodenough, *Phys. Rev.*, 1955, **100**, 564–573.
- 686 59 D. Goldfarb and S. Stoll, *EPR Spectroscopy: Fundamentals and Methods*, WILEY, 2018.
- 687 60 H. A. F. Charles P. Poole Jr., *Theory of Magnetic Resonance*, WILEY, 2nd edn., 1987.
- 688 61 S. Li, L. Shi, Y. Guo, J. Wang, D. Liu and S. Zhao, *Chem. Sci.*, 2024, **15**, 11188–11228.
- 689 62 Y. Wang, J. Qian, J. Zheng, J. Li, A. Sun, J. Xing, L. Liu and Y. Zheng, *J. Alloy. Compd.*,
690 2024, **1004**, 175821.
- 691 63 Y. Zheng, S. Chen, X. Yu, K. Li, X. Ni and L. Ye, *Appl. Surf. Sci.*, 2022, **598**, 153786.
- 692 64 J. Xu, Z. Zhou, T. Yang, X. Liu, G. Tang, H. Wu, D. Zhang, Y. Su, Z. Wu, Z. Pei and W.
693 Yang, *Adv. Mater.*, 2025, **37**, e12724.
- 694 65 X. Liu, F. Zhan, D. Li and M. Xue, *Int. J. Hydrog. Energy*, 2020, **45**, 28836–28846.
- 695 66 C. Xie, W. Chen, S. Du, D. Yan, Y. Zhang, J. Chen, B. Liu and S. Wang, *Nano Energy*, 2020,
696 **71**, 104653.
- 697 67 M. E. G. Lyons and M. P. Brandon, *J. Electroanal. Chem.*, 2009, **631**, 62–70.



- 698 68 A. C. Lazanas and M. I. Prodromidis, *ACS Meas. Sci. Au*, 2023, **3**, 162–193.
- 699 69 X. Zou, Q. Lu, J. Wu, K. Zhang, M. Tang, B. Wu, S. She, X. Zhang, Z. Shao and L. An, *Adv. Funct. Mater.*, 2024, **34**, 1–11.
- 700
- 701 70 S. Yadav and N. Kurra, *Energy Storage Mater.*, 2024, **65**, 103094.
- 702 71 S. F. Hung, Y. Y. Hsu, C. J. Chang, C. S. Hsu, N. T. Suen, T. S. Chan and H. M. Chen, *Adv. Energy Mater.*, 2018, **8**, 1–11.
- 703
- 704 72 L. Zhuang, Y. Jia, H. Liu, X. Wang, R. K. Hocking, H. Liu, J. Chen, L. Ge, L. Zhang, M. Li, C. L. Dong, Y. C. Huang, S. Shen, D. Yang, Z. Zhu and X. Yao, *Adv. Mater.*, 2019, **31**, 1805581.
- 705
- 706
- 707 73 F. T. Haase, A. Bergmann, T. E. Jones, J. Timoshenko, A. Herzog, H. S. Jeon, C. Rettenmaier and B. R. Cuenya, *Nat. Energy*, 2022, **7**, 765–773.
- 708
- 709 74 J. Huang, A. H. Clark, N. Hales, K. Crossley, J. Guehl, R. Skoupy, T. J. Schmidt and E. Fabbri, *Nat. Chem.*, 2025, **17**, 856–864.
- 710
- 711 75 J. Ma, Q. Wu, W. Zhang, Y. Li, Y. Lu, B. Liu, F. Yang and Y. Song, *Electrochim. Acta*, 2022, **432**, 141224.
- 712
- 713 76 Y. Bai, Y. Wu, X. Zhou, Y. Ye, K. Nie, J. Wang, M. Xie, Z. Zhang, Z. Liu, T. Cheng and C. Gao, *Nat. Commun.*, 2022, **13**, 6094.
- 714
- 715 77 S. Liu, B. Zhang, Y. Cao, H. Wang, Y. Zhang, S. Zhang, Y. Li, H. Gong, S. Liu, Z. Yang and J. Sun, *ACS Energy Lett.*, 2023, **8**, 159–168.
- 716
- 717 78 J. K. Nørskov, J. Rossmeisl, A. Logadottir, L. Lindqvist, J. R. Kitchin, T. Bligaard and H. Jónsson, *J. Phys. Chem. B*, 2004, **108**, 17886–17892.
- 718
- 719 79 M. Li, S. Zhou and M. Xu, *Chem. Eng. J.*, 2017, **328**, 106–116.
- 720 80 B. L. Lai, Z. H. Xiao, P. Y. Jiang, Y. Xie, N. Li and Z. Q. Liu, *ChemElectroChem*, 2022, **9**, e202101699.
- 721
- 722 81 H. Zhu, Z. Zhang, Y. Zhou, X. Jiang, F. Cai, Y. Bai and H. Ning, *J. Water Process Eng.*, 2022, **45**, 102471.
- 723
- 724 82 J. Liu, C. Chu, L. Wei, J. Feng and J. Shen, *Biosens Bioelectron.*, 2023, **222**, 114926.
- 725

View Article Online
DOI: 10.1039/D6TA03240K



The data will be available upon reasonable request.

